remote sensing

MDPI

Article

A Study on the Classification of Shrubs and Grasses on the Tibetan Plateau Based on Unmanned Aerial Vehicle Multispectral Imagery

Xiaoqiang Chen [1], Hui Deng [1,*], Wenjiang Zhang [1] and Houxi Zhang [2]

[1] College of Geography and Planning, Chengdu University of Technology, Chengdu 610059, China; 2022020187@stu.cdut.edu.cn (X.C.); zhangwenjiang13@cdut.edu.cn (W.Z.)
[2] College of Forestry, Fujian Agriculture and Forestry University, Fuzhou 350002, China; zhanghouxi@fafu.edu.cn
* Correspondence: dengh@cdut.edu.cn

Abstract: The ecosystem of the Qinghai–Tibet Plateau is highly fragile due to its unique geographical conditions, with vegetation playing a crucial role in maintaining ecological balance. Thus, accurately monitoring the distribution of vegetation in the plateau region is of paramount importance. This study employs UAV multispectral imagery in combination with four machine-learning models—Support Vector Machine (SVM), Decision Tree (DT), Extreme Gradient Boosting (XGBoost), and Random Forest (RF)—to investigate the impact of different features and their combinations on the fine classification of shrubs and grasses on the Qinghai–Tibet Plateau, including *Salix psammophila*, *Populus simonii Carrière*, *Kobresia tibetica*, and *Kobresia pygmaea*. The results indicate that near-infrared spectral information can improve classification accuracy, with improvements of 5.21%, 1.65%, 6.64%, and 5.03% for *Salix psammophila*, *Populus simonii Carrière*, *Kobresia tibetica*, and *Kobresia pygmaea*, respectively. Feature selection effectively reduces redundant information and enhances model classification accuracy, with all four machine-learning models achieving the best performance on the optimized feature set. Furthermore, the RF model performs best on the optimized feature set, achieving an overall accuracy (OA) of 95.32% and a kappa coefficient of 0.94. This study provides important scientific support for the fine classification and ecological monitoring of plateau vegetation.

Keywords: UAV remote sensing; OBIA; feature optimization; Tibetan Plateau; vegetation classification

check for updates

Citation: Chen, X.; Deng, H.; Zhang, W.; Zhang, H. A Study on the Classification of Shrubs and Grasses on the Tibetan Plateau Based on Unmanned Aerial Vehicle Multispectral Imagery. *Remote Sens.* **2024**, *16*, 4106. https://doi.org/10.3390/rs16214106

Academic Editor: Javier Marcello

Received: 9 October 2024
Revised: 29 October 2024
Accepted: 31 October 2024
Published: 2 November 2024

Copyright: © 2024 by the authors. Licensee MDPI, Basel, Switzerland. This article is an open access article distributed under the terms and conditions of the Creative Commons Attribution (CC BY) license (https://creativecommons.org/licenses/by/4.0/).

1. Introduction

Vegetation, as the foundation of terrestrial ecosystems, plays an indispensable role in maintaining ecological balance, regulating climate, conserving soil and water resources, and supporting biodiversity [1–3]. The unique climate and geographical conditions of the Tibetan Plateau have nurtured a rich diversity of vegetation types, which play a crucial role in regulating regional water cycles, mitigating climate change, and preventing land degradation [4–6]. The vulnerability of the plateau ecosystem makes the monitoring and study of its vegetation particularly important, not only for revealing the structure and function of the plateau ecosystem but also for addressing global climate change and regional ecological management.

Traditional methods for surveying plateau vegetation primarily rely on manual ground surveys, which suffer from low efficiency, high costs, and difficulties in obtaining large-scale, objective data [7–9]. With the rapid development of remote-sensing technology, satellite data have gradually become an important tool for plateau vegetation monitoring. Although studies based on medium- and low-resolution satellite data, such as those by Bazhuoma [10], who investigated the distribution of typical vegetation on the northern Tibetan Plateau based on MODIS satellite data, and Zhang [11], who used MOD13Q1_VC data for vegetation classification on the Qinghai–Tibet Plateau, have made significant progress, these methods still

face considerable limitations in meeting the demands for high-precision, real-time vegetation classification due to constraints in satellite resolution, weather influences, and data timeliness [12]. In contrast, UAV remote sensing, with its advantages of high resolution, flexibility, and low cost, has become an ideal choice for high-precision, real-time vegetation monitoring, especially in small-scale ecosystem studies [13–17].

Remote-sensing image classification methods are divided into pixel-based and object-based methods. Traditional pixel-based methods mainly rely on the spectral information of individual pixels, which are prone to noise, leading to misclassification or omission [18]. To address this issue, object-based image analysis (OBIA) techniques have been gradually introduced to more effectively handle high-resolution remote-sensing images [19]. OBIA methods improve classification accuracy and reduce "salt-and-pepper" noise by incorporating multiple features such as texture and spectral information from neighboring pixels within objects [20,21]. Previous studies have demonstrated that combining OBIA with machine-learning algorithms can significantly enhance classification performance. For instance, She et al. [22] achieved a high classification accuracy of 87.77% in desert grassland vegetation classification using the Random Forest (RF) algorithm, while Geng et al. [23] used an object-oriented Random Forest algorithm for vegetation identification in the Huixian Wetland, achieving an overall accuracy of 86.75%, with user accuracy exceeding 90% for various vegetation communities in a typical karst wetland. Na et al. [24] applied object-oriented image analysis technology and pixel-based supervised classification methods for desert grassland plant species identification, finding that the object-oriented image analysis outperformed the pixel-based supervised classification in terms of accuracy. Yang et al. [25] combined OBIA with machine-learning algorithms for urban green space extraction, showing that OBIA effectively mitigated "salt-and-pepper" noise and outperformed pixel-based methods. However, research on the application of OBIA combined with machine-learning models in the complex environment of the plateau remains limited, particularly concerning the impact of near-infrared spectra on vegetation classification accuracy. Based on this, the present study focuses on the classification of typical vegetation on the Qinghai–Tibet Plateau. Utilizing unmanned aerial vehicle (UAV) multispectral imagery as the data source and combining it with object-based image analysis (OBIA) methods, we aim to distinguish four common types of highland vegetation. This vegetation not only serves as an indicator of the health of the plateau's ecosystem but also plays a significant role in addressing local environmental issues and preventing land desertification [26].

To enhance classification accuracy, this study employs four machine-learning models: Support Vector Machine (SVM), Decision Tree (DT), Random Forest (RF), and Extreme Gradient Boosting (XGBoost), all integrated with the OBIA approach. SVM is suitable for classification tasks in high-dimensional feature spaces and can handle nonlinear boundary problems, although its efficiency may be limited with large datasets [27]. The DT model is intuitive and interpretable but may be susceptible to noise, potentially leading to overfitting [28]. RF reduces the risk of overfitting by integrating multiple decision trees and performs well in handling complex feature combinations [29]. Meanwhile, XGBoost optimizes classification accuracy and generalization capabilities through gradient boosting and is highly efficient for large-scale datasets [30].

Therefore, this study combines various machine-learning models with the OBIA method to classify highland vegetation, exploring the effects of visible and near-infrared spectral features and their combinations on vegetation classification. Through cross-validation among multiple models, we clarify the contributions of various visible and near-infrared spectral features to the identification of different highland vegetation types. By selecting and evaluating different feature subsets, we further optimize the classification accuracy of the models. This research provides effective technical support for the fine classification of highland vegetation and establishes a scientific basis for monitoring and protecting the plateau's ecosystem.

2. Materials and Methods

2.1. Study Area

The study area is located in Lazi County, Shigatse City, Tibet Autonomous Region, China, with a total area of approximately 61,037.27 square meters. Lazi County has a complex and diverse terrain. Influenced by factors such as topography and high-altitude air circulation, a warm, humid, semi-arid climate characterized by low precipitation, cool summers, cold winters, intense sunlight, and significant vertical variation is observed. The soil in this area is classified into shrub steppe soil, alpine steppe soil, subalpine meadow soil, and alpine meadow soil. Along the river valleys, there are shrub communities dominated by Sophora moorcroftiana and grasses; in mountainous areas, due to aridity, strong gravel content, and poor soil, only a few species grow, such as *Salix psammophila*, *Populus simonii Carrière*, and alpine meadow vegetation dominated by *Kobresia tibetica*, *Kobresia pygmaea*, and Carex spp. [26]. The geographical location of the study area is shown in Figure 1.

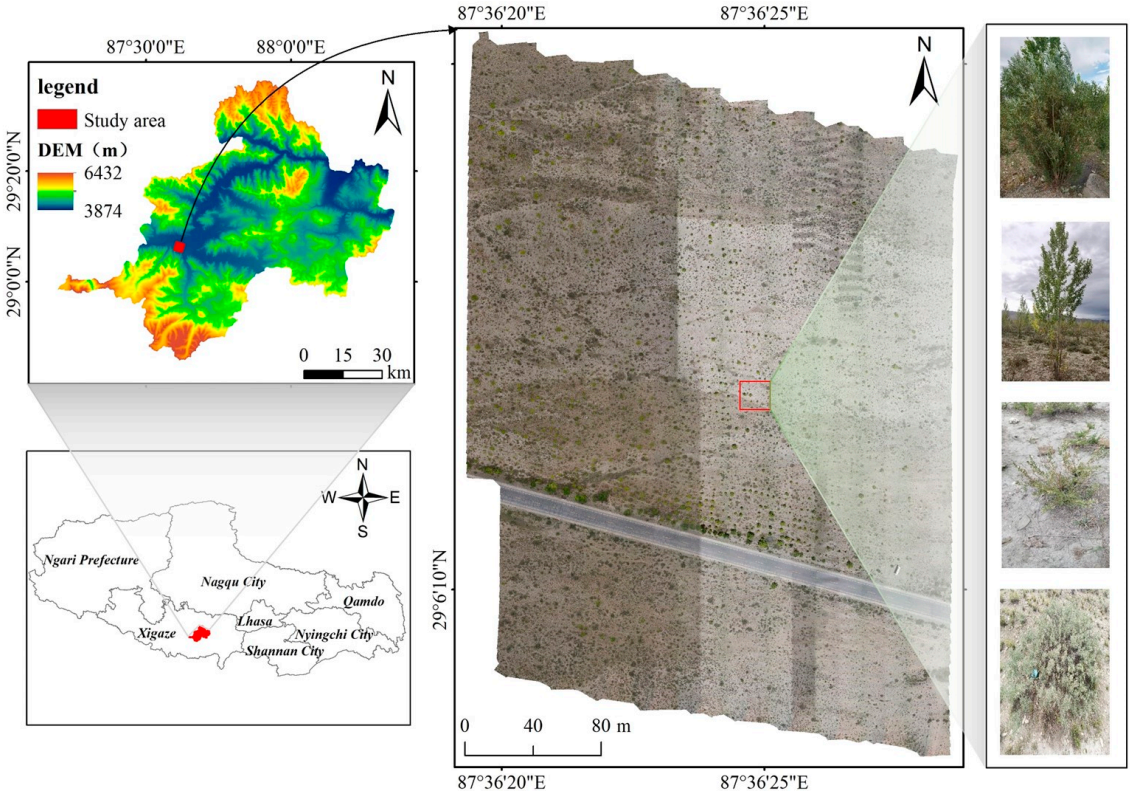


Figure 1. Location of the study area.

2.2. Data Acquisition and Preprocessing

In this study, remote-sensing images were collected using a DJI Phantom 4 Multispectral drone (China). The drone is equipped with one color sensor and five multispectral monochrome sensors, with an effective pixel count of 2.08 million per sensor. Data were collected in August 2022 at a flight altitude of 35 m, a speed of 3 m/s, and a shooting interval of 2 s, with a forward overlap rate of 75% and a lateral overlap rate of 60%. The resolution of the generated images is uniformly 1600 × 1300 pixels. A total of 4527 aerial images were collected under clear and cloudless conditions. Using DJI Terra V4.3.0 software, an orthomosaic (DOM) and a digital surface model (DSM) were generated [31]. The Ground Sampling Distance (GSD) of the orthomosaic (DOM) is 0.17 m, while the resolution of the digital surface model (DSM) is 0.39 m in the x-direction and 0.32 m in the y-direction. Subsequently, decorrelation stretching (ENVI 5.6) was applied to the images to enhance them by eliminating high correlations in the data while retaining chromaticity information, further highlighting color differences in the features, which helps improve classification accuracy.

2.3. Field Survey and Selection of Classification Samples

To study the spectral characteristics and spatial distribution patterns of different types of alpine vegetation, ten 10 m × 10 m plots were randomly laid out within the study area for vegetation population statistical analysis. Based on the results of the vegetation survey, the study classified the primary vegetation in the area, including four vegetation types: *Salix psammophila*, *Populus simonii Carrière*, *Kobresia tibetica*, and *Kobresia pygmaea*. Additionally, non-vegetation land cover types such as bare soil and roads were also included in the study, as shown in Figure 2.

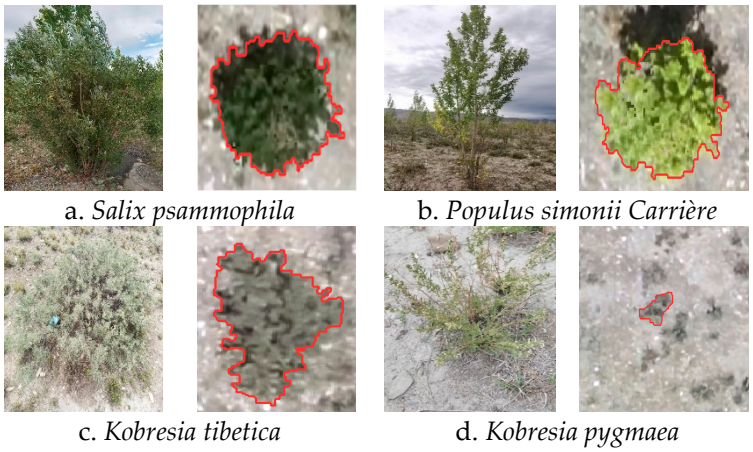


Figure 2. Sample images of ground objects.

Based on the distribution of land cover in the study area and visual interpretation, six representative land cover types were selected from the images, comprising 2350 samples (including 157 for *Salix psammophila*, 405 for *Populus simonii Carrière*, 365 for *Kobresia tibetica*, 346 for *Kobresia pygmaea*, 186 for roads, and 891 for bare soil). In the experiment, a 7:3 ratio was used to split the samples into training and validation datasets for detailed vegetation classification [32]. The distribution of land cover sample sets is shown in Table 1.

Table 1. Training and validation sample sets.

Land Cover Types	Total Number of Samples	Training Dataset	Validation Dataset
Salix psammophila	157	110	47
Populus simonii Carrière	405	277	128
Kobresia tibetica	365	256	109
Kobresia pygmaea	346	230	116
Bare Soil	891	637	254
Roads	186	135	51
Total	2350	1645	705

2.4. Image Segmentation

A crucial step in OBIA is image segmentation, as the results directly affect the extraction accuracy of object-based algorithms [33]. To this end, many researchers use the Estimation of Scale Parameter 2 (ESP2) tool to obtain the optimal segmentation parameters for images. This tool determines the optimal segmentation parameters by calculating the rates of change of local variations (LVs) in the homogeneity of objects at different segmentation scales (ROC-LV). Therefore, the local optimal segmentation scale is obtained when the ROC of LVs reaches a local maximum value [34]. In this study, eCognition 9.0 with the ESP2 plugin was used to determine the optimal segmentation scale and segment the images. Through research, the shape factor and compactness factor were set to 0.7 and 0.3, respectively. The changes in LVs and ROC under different segmentation scale parameters are shown in Figure 3. The local

optimal scale is obtained when the ROC reaches its peak. Based on this, the local optimal scales chosen in this study were 30, 36, 50, 60, 80, 98, and 114.

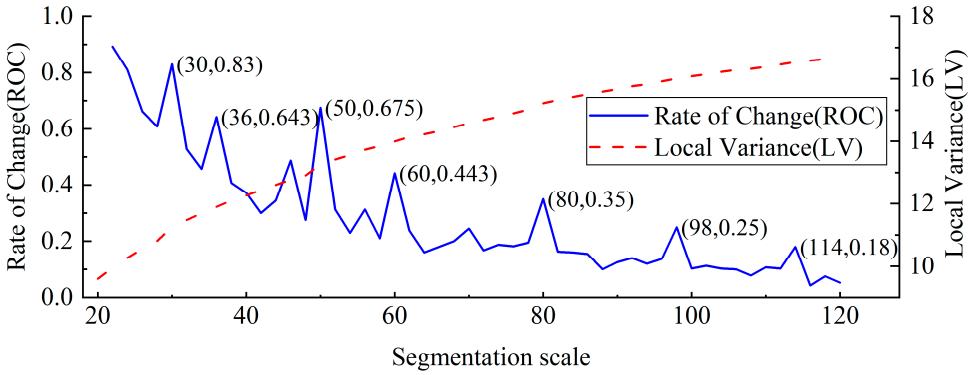


Figure 3. ESP2 segmentation scale parameter estimation chart.

The segmentation results at the local optimal scale are shown in Figure 4. Experimental comparisons indicate that when the segmentation scale exceeds 60 (e.g., d. 60, e. 80, f. 98, and g. 114), *Kobresia tibetica*, *Kobresia pygmaea*, and bare soil are prone to under-segmentation, which causes vegetation and bare soil to occur in the same patch. Conversely, when the segmentation scale is less than 50 (e.g., a. 30 and b. 36), excessive segmentation leads to overly fragmented land cover, particularly affecting *Salix psammophila*, *Populus simonii Carrière*, and *Kobresia tibetica*. Based on a comprehensive comparison of segmentation results at various scales, the optimal segmentation scale for this study was determined to be 50.

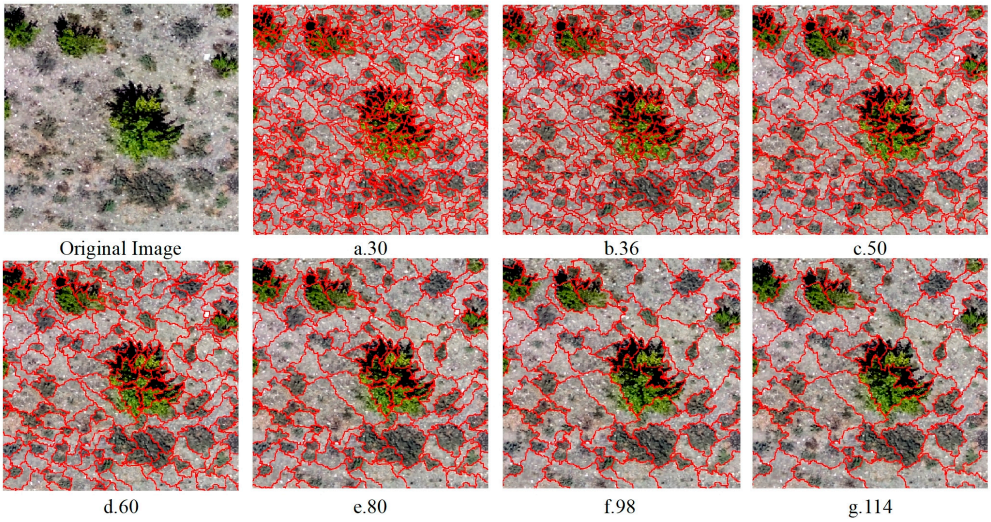


Figure 4. Illustration of different segmentation scales. (**a**) Segmentation scale of 30, (**b**) Segmentation scale of 36, (**c**) Segmentation scale of 50, (**d**) Segmentation scale of 60, (**e**) Segmentation scale of 80, (**f**) Segmentation scale of 98, (**g**) Segmentation scale of 114.

2.5. Feature Extraction

The features selected in this study include spectral features, index features, height features, and texture features, as detailed below:

(1) Spectral features (SPEC): This includes seven features: red band (R), green band (G), blue band (B), maximum difference between bands (Max_diff), brightness value (Brightness), near-infrared band (NIR), and red-edge band (RedEdge) [35].

(2) Index features (INDE): Visible light indices include the Green–Blue Ratio Index (GBRI), Red–Green Ratio Index (RGRI), Excess Green Minus Excess Red Index (EXGR), and

Differential Enhanced Vegetation Index (DEVI), as listed in Table 2. Near-infrared indices include the Normalized Difference Vegetation Index (NDVI), Ratio Vegetation Index (RVI), Enhanced Vegetation Index (EVI), Green Normalized Difference Vegetation Index (GNDVI), and Nonlinear Vegetation Index (NLI), as listed in Table 3.

Table 2. Formulas for visible light indices.

Index Features	Formulas	Reference
GBRI	B/G	[36]
RGRI	R/G	[37]
EXGR	$(2 \times G - R - B) - (1.4 \times R - B)$	[38]
DEVI	$(G + R + B)/3 \times G$	[39]

Table 3. Formulas for near-infrared indices.

Index Features	Formulas	Reference
NDVI	$(NIR - R)/(NIR + R)$	[40]
RVI	R/NIR	[41]
EVI	$2.5 \times ((NIR - R)/(NIR + 6 \times R - 7.5 \times B + 1))$	[42]
GNDVI	$(NIR - G)/(NIR + G)$	[43]
NLI	$(NIR2 - R)/(NIR2 + R)$	[44]

(3) Height feature (HEIG): The normalized digital surface model (nDSM) is an elevation model that reflects the absolute height of ground objects, providing reliable data for object discrimination [45]. In this study, ArcMap 10.5 software was used to extract terrain features. First, 4622 ground points were manually selected from the DSM through visual interpretation, and the elevation information of the raster was extracted in batches. Next, the Kriging interpolation method was employed to generate the Digital Elevation Model (DEM). Finally, the DSM was subtracted from the DEM using the Raster Calculator to obtain the nDSM [46].

(4) Texture feature (GLCM): Texture features reflect the texture information of local image regions and are typically represented by the Gray-Level Co-Occurrence Matrix (GLCM) [47]. In this study, eight feature values were selected: mean, standard deviation (GLCM-SD), homogeneity, dissimilarity, angular second moment (GLCM-ASM), entropy, correlation, and contract. The texture features and corresponding formulas are shown in Table 4.

Table 4. Texture feature formulas.

Texture Feature	Formula	Reference
Mean	$\sum_{i=0}^{quant_k} \sum_{j=0}^{quant_k} p(i,j) \times i$	[48]
Standard Deviation	$\sqrt{\sum_{i=0}^{quant_k} \sum_{j=0}^{quant_k} p(i,j) \times (i - Mean)^2}$	[49]
Homogeneity	$\sum_{i=0}^{quant_k} \sum_{j=0}^{quant_k} p(i,j) \times \frac{1}{1 + (i+j)^2}$	[50]
Dissimilarity	$\sum_{i=0}^{quant_k} \sum_{j=0}^{quant_k} p(i,j) \times \lvert i - j \rvert$	[51]
Angular Second Moment	$\sum_{i=0}^{quant_k} \sum_{j=0}^{quant_k} p(i,j)^2$	[52]
Entropy	$\sum_{i=0}^{quant_k} \sum_{j=0}^{quant_k} p(i,j) \times \ln p(i,j)$	[53]
Correlation	$\sum_{i=0}^{quant_k} \sum_{j=0}^{quant_k} \frac{(i - Mean) \times (j - Mean) \times p(i,j)^2}{Variance}$	[54]
Contract	$\sum_{i=0}^{quant_k} \sum_{j=0}^{quant_k} p(i,j) \times (i - j)^2$	[55]

2.6. Experimental Design

This study designed eight experimental schemes (S1–S8) to compare the impact of spectral, height, index, and texture features on the classification of different vegetation types in the study area using algorithms such as Support Vector Machine (SVM), Decision Tree (DT), Random Forest (RF), and Extreme Gradient Boosting (XGBoost). Specifically, S1 consists of only 5 features, including the R, G, and B bands, maximum spectral difference, and brightness values. S2 to S7 are based on S1 with the addition of height features, near-infrared bands, red-edge bands, visible light indices, near-infrared indices, and texture features, respectively. S8 applies the Recursive Feature Elimination (RFE) algorithm to remove redundant features from all features. Detailed information on the schemes is presented in Table 5.

Table 5. Classification schemes for different feature combinations.

Program	Feature Set	Number of Features
S1	R, G, B, Max_diff, Brightness	5
S2	R, G, B, Max_diff, Brightness, nDSM	6
S3	R, G, B, Max_diff, Brightness, nDSM, NIR, RedEdge	8
S4	R, G, B, Max_diff, Brightness, NIR, RedEdge, nDSM, GBRI, RGRI, EXGR, DEVI	12
S5	R, G, B, Max_diff, Brightness, NIR, RedEdge, nDSM, NDVI, RVI, EVI, GNDVI, NLI	13
S6	R, G, B, Max_diff, Brightness, NIR, RedEdge, nDSM, GBRI, RGRI, EXGR, DEVI, NDVI, RVI, EVI, GNDVI, NLI	17
S7	R, G, B, Max_diff, Brightness, NIR, RedEdge, nDSM, GBRI, RGRI, EXGR, DEVI, NDVI, RVI, EVI, GNDVI, NLI, Mean, GLCM-SD, Homogeneity, Dissimilarity, GLCM-ASM, Entropy, Correlation, Contract	25
S8	Optimal feature set	21

2.7. Accuracy Evaluation Metrics

Classification accuracy is typically quantitatively assessed using a confusion matrix [56]. To comprehensively evaluate the classification performance of different feature combinations under various algorithms, this study calculates four key metrics derived from the confusion matrix: overall accuracy (OA) (presented in Equation (1)), producer's accuracy (PA) (presented in Equation (2)), user's accuracy (UA), (presented in Equation (3)), and the kappa coefficient (presented in Equation (4)). These metrics provide a multi-dimensional assessment of the classification results. Overall accuracy (OA) reflects the overall correct classification rate across all categories, offering an overview of the model's overall performance. Producer's accuracy (PA) represents the probability that a certain category is correctly classified, reflecting the model's ability to recognize that category and avoid omissions. User's accuracy (UA), from the user's perspective, measures the reliability of the classification by indicating how accurately the model predicts a given category. The kappa coefficient further examines the agreement between the model's classification and the true classification, accounting for chance agreement. Compared to OA, the kappa coefficient offers a more comprehensive and objective evaluation of the classification result's reliability. These four metrics collectively provide an in-depth analysis of classification performance, revealing the differences in how various feature combinations and algorithms perform in classification tasks.

$$OA = \frac{\sum_{i=1}^{n} TP_i}{N} \quad (1)$$

$$PA_i = \frac{TP_i}{TP_i + FN_i} \quad (2)$$

$$UA_i = \frac{TP_i}{TP_i + FP_i} \quad (3)$$

$$k = \frac{OA - P_e}{1 - P_e} \quad (4)$$

$$P_e = \frac{1}{N^2}\sum_{i=1}^{n}(TP_i + FN_i) \times (TP_i + FP_i) \quad (5)$$

where TP_i is the number of correctly classified samples for category i, N is the total number of samples, FN_i represents the number of missed samples for category i, and FP_i indicates the number of misclassified samples for category i.

3. Results

3.1. Feature Selection Results

Noise and redundant features can lead to overfitting in supervised learning models, thus reducing model accuracy [57]. Therefore, this study utilizes PyCharm Community Edition software and employs RFE to select 25 features. As shown in Figure 5, the classification accuracy of the RF model gradually increased with the number of features, peaking at 21 features before declining. This indicates that while the increase in feature numbers enhances the classification accuracy, it also introduces more noise and redundant features. To optimize model performance, the top 21 features with the highest contribution were selected as the optimal feature set (see Figure 6**).**

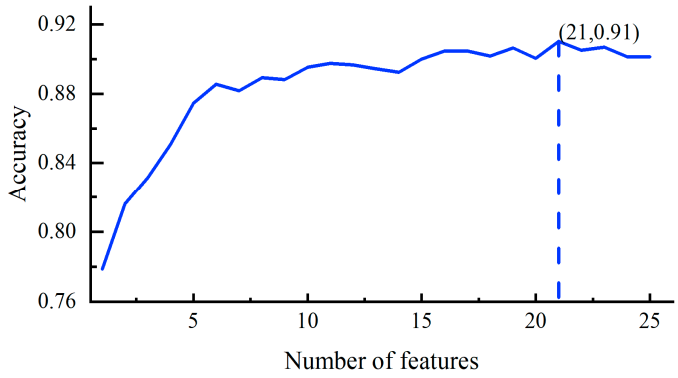


Figure 5. Relationship between classification accuracy and number of features.

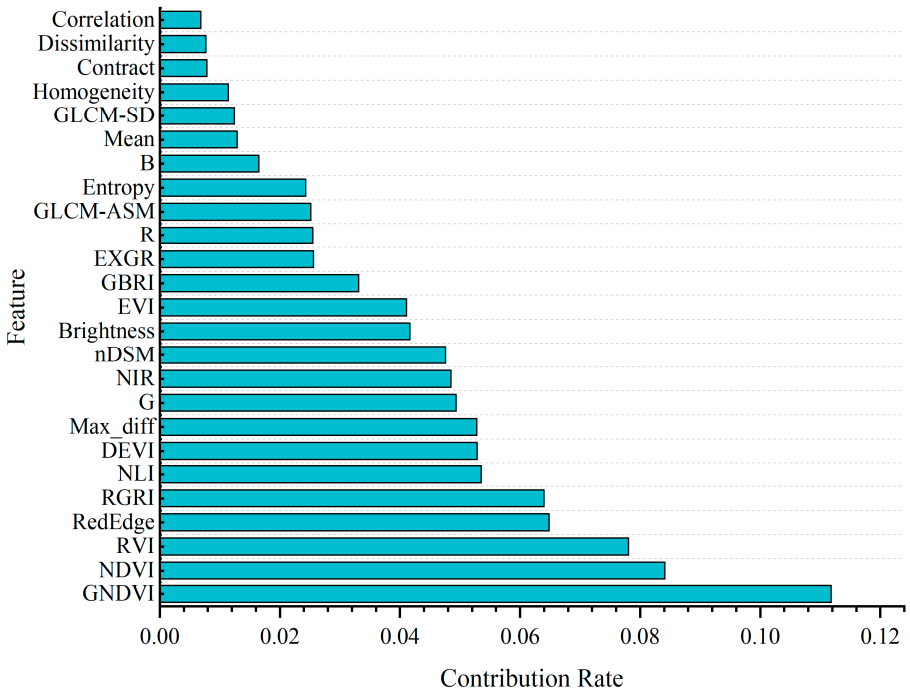


Figure 6. Contribution rate of features.

3.2. Accuracy Evaluation of Different Feature Combinations

This study evaluated the impact of different features and their combinations on plateau vegetation classification using four models: SVM, DT, RF, and XGBoost. As can be seen from Table 6 and Figure 7, the overall classification accuracy (OA) consistently improved with the increase in the number of features. S1, which used only visible light spectral features, had the lowest accuracy, with OA values of 80.69%, 84.40%, 89.79%, and 89.93% for SVM, DT, RF, and XGBoost, respectively. In S2, where height features were added, the PA of *Salix psammophila*, bare soil, and *Kobresia tibetica* increased by 0.23% to 4.51%, while the PA of *Populus simonii Carrière*, roads, and *Kobresia pygmaea* decreased by 3.87% to 4.77%. The UA and OA increased by 1.43% and 0.42%, respectively, as HEIG reflects the height relationships of different ground objects but is redundant for objects with small height differences. In S3, which added near-infrared features to S2, the PA of *Populus simonii Carrière* and roads increased by 5.4% and 4.81%, respectively, while UA and OA increased by 0.30% and 0.35%, respectively, indicating that near-infrared features can effectively improve the classification of *Populus simonii Carrière* due to its distinct near-infrared characteristics compared to other objects. S4, which added visible light indices to S3, saw increases in PA for *Kobresia tibetica*, *Kobresia pygmaea*, *Populus simonii Carrière*, and roads by 0.36% to 4.01%, while the PA of *Salix psammophila* decreased by 1.52%. UA and OA increased by 1.05% and 0.93%. The visible light index has a significant impact on the model's identification of various ground objects in the study area and plays an important role in improving the classification accuracy of the model. In S5, which added near-infrared indices to S3, the PA of *Kobresia pygmaea*, *Populus simonii Carrière*, bare soil, and roads all increased, with the highest increase seen in *Kobresia pygmaea* at 7.67%. However, the PA of *Salix psammophila* and *Kobresia tibetica* decreased by 1.42% and 0.21%, respectively. Compared to S4, the PA of *Salix psammophila*, bare soil, and *Populus simonii Carrière* improved, with *Kobresia pygmaea* showing the largest increase of 7.31%, but the PA of *Kobresia tibetica* and roads declined by 4.23% and 2.71%, respectively. UA and OA increased by 0.91% and 0.6%. Compared to S4, the near-infrared index provided a greater boost to classification accuracy, especially for *Kobresia pygmaea*, while the visible light index contributed more to the classification of *Kobresia tibetica* and roads. In S6, compared to S3, the PA of all vegetation types significantly improved, with *Kobresia pygmaea* seeing the largest increase at 9.08%, while *Salix psammophila*, *Kobresia tibetica*, and *Populus simonii Carrière* improved by 3.15%, 1.65%, and 5.03%, respectively. UA increased by 3.50%, and OA improved by 2.24%. Compared to S4, the PA of *Salix psammophila*, *Kobresia pygmaea*, and *Populus simonii Carrière* increased by 4.67%, 8.72%, and 3.32%, respectively, with UA increasing by 2.45% and OA improving by 1.31%. Compared to S5, the PA of *Salix psammophila*, *Kobresia tibetica*, *Kobresia pygmaea*, and *Populus simonii Carrière* increased by 4.57%, 1.86%, 1.41%, and 3.25%, respectively, with UA increasing by 1.54% and OA improving by 0.71%. These results indicate that the high-dimensional feature combination of visible light and near-infrared indices provides more effective information and significantly enhances model classification accuracy. In S7, which added texture features to S6, the PA of *Kobresia pygmaea* and *Populus simonii Carrière* decreased significantly, while the PA of other objects increased only slightly. Additionally, UA and OA fluctuated, with ranges of −3.45% to 1.38% and −0.85% to 0.57%, respectively. This suggests that while high-dimensional feature combinations can provide more information, they also introduce more noise and redundant information, thus affecting model classification performance. Compared to S7, the optimal feature set in S8 showed varying degrees of improvement in the PA of all objects, with increases ranging from 0.74% to 3.07%, while UA and OA improved overall by 2.13% and 1.78%. This demonstrates that feature selection can effectively reduce dimensionality and optimize high-dimensional datasets, allowing the model to maintain high classification accuracy with fewer features.

Table 6. Classification accuracy evaluation.

Classifier	Scheme	*Salix psammophila*		Bare Soil		*Kobresia tibetica*		*Kobresia pygmaea*		*Populus simonii Carrière*		Roads		OA
		PA	UA	PA	UA	PA	UA	PA	UA	PA	UA	PA	UA	
SVM	S1	68.89	62.00	83.90	84.62	86.61	82.91	59.09	61.32	86.95	90.91	91.38	88.33	80.69
	S2	66.67	68.19	85.17	83.75	89.29	77.52	54.72	56.31	88.41	94.57	85.48	96.36	80.69
	S3	63.04	70.73	85.23	82.79	84.82	78.51	52.78	57.00	92.75	93.43	91.94	95.00	80.80
	S4	57.14	70.59	86.79	84.25	91.96	75.18	46.43	59.09	92.24	93.04	96.55	96.55	81.13
	S5	70.83	77.27	86.82	82.66	90.35	87.29	47.00	50.54	90.83	90.08	89.23	1.00	81.56
	S6	74.42	84.21	84.84	84.23	90.38	80.34	52.10	58.49	94.92	93.33	93.18	91.11	81.70
	S7	69.57	74.42	88.97	86.35	91.23	79.39	48.65	60.67	88.98	88.98	96.23	96.23	82.27
	S8	65.96	86.11	89.37	83.46	95.41	83.87	50.86	66.29	96.09	93.18	98.04	96.15	84.26
DT	S1	65.90	58.00	91.15	94.80	83.33	77.87	72.12	74.26	84.80	87.60	91.38	86.89	84.40
	S2	66.67	62.96	93.47	93.82	83.64	80.00	83.84	74.75	79.65	90.91	83.93	92.17	85.67
	S3	60.87	59.57	94.09	91.39	86.61	81.51	75.45	81.37	83.33	87.79	90.32	90.32	85.69
	S4	59.52	64.10	94.34	89.93	88.39	86.84	70.54	83.16	89.66	88.89	93.10	87.10	86.67
	S5	64.58	58.49	96.12	93.94	81.58	89.42	81.00	81.82	85.83	88.03	95.38	91.18	87.66
	S6	67.44	72.50	93.50	95.22	85.58	83.96	83.19	81.15	92.37	90.08	90.91	90.91	88.65
	S7	66.67	69.77	94.70	93.28	90.35	85.12	73.87	84.53	87.29	86.55	96.23	89.47	87.80
	S8	72.34	69.39	96.06	94.57	90.83	81.15	75.86	88.89	87.50	90.32	98.04	94.34	88.94
RF	S1	70.45	68.89	95.77	96.89	80.70	91.09	90.38	79.00	90.40	89.68	93.10	94.74	89.79
	S2	70.59	73.45	97.46	94.71	88.18	87.38	86.87	81.13	84.96	94.12	91.07	96.23	90.07
	S3	69.57	74.42	98.73	94.74	87.50	88.29	81.82	82.57	89.86	92.54	96.77	98.36	90.50
	S4	66.67	77.78	97.74	95.22	91.96	91.15	86.61	88.18	92.24	92.24	98.28	98.28	92.34
	S5	64.58	83.78	98.06	97.31	87.72	93.45	92.00	82.88	95.00	89.06	95.38	1.00	92.48
	S6	72.09	83.78	98.56	95.79	88.46	95.83	92.44	88.00	95.76	92.62	90.91	1.00	93.48
	S7	71.11	82.05	98.11	97.37	91.23	93.69	91.89	88.70	92.37	90.83	1.00	98.15	93.48
	S8	74.47	87.50	99.21	99.21	96.33	91.30	92.24	93.68	96.09	93.89	98.04	98.04	95.32
XGBoost	S1	72.73	71.11	93.46	96.81	83.33	94.06	91.35	77.87	90.40	91.13	96.55	90.32	89.93
	S2	72.55	74	97.10	94.04	90.91	90.91	83.84	82.18	84.07	91.35	92.86	94.55	90.07
	S3	71.74	76.74	97.47	95.06	89.29	88.50	82.73	85.05	92.75	93.43	93.55	93.55	90.92
	S4	71.43	76.92	96.23	94.44	91.96	87.29	83.93	90.38	91.38	93.81	98.29	93.44	91.49
	S5	68.75	80.49	98.06	97.31	87.72	91.74	90.00	84.11	94.17	90.40	95.38	98.41	92.34
	S6	72.09	81.58	96.75	96.06	90.38	94.95	91.60	87.20	95.76	97.62	93.18	97.62	93.05
	S7	73.33	82.50	98.48	95.54	89.47	95.33	90.09	86.21	93.22	91.67	94.34	98.04	92.91
	S8	74.47	85.37	99.61	98.83	94.50	91.15	91.38	92.98	95.31	93.85	1.00	1.00	95.04

Note: The producer's accuracy (PA), user's accuracy (UA), and overall accuracy (OA) are all expressed as percentages.

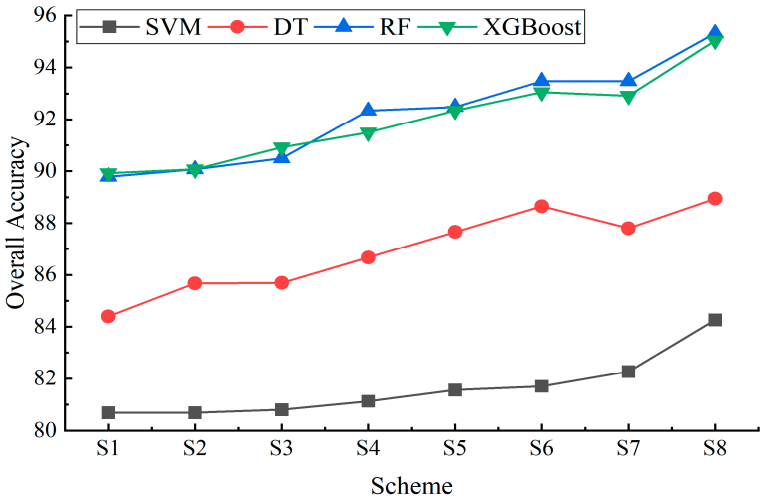


Figure 7. Overall accuracy of each model for schemes S1 to S8.

3.3. Accuracy Evaluation of Different Classification Methods Based on Optimal Features

The classification accuracy of four machine-learning algorithms—Support Vector Machine (SVM), Decision Tree (DT), Random Forest (RF), and Extreme Gradient Boosting (XGBoost)—was compared based on the optimal feature set. The results, shown in Table 7, indicate that among the four algorithms, RF performed the best, with an overall accuracy (OA) of 95.32% and a kappa coefficient of 0.94. Compared to SVM, DT, and XGBoost, RF's OA improved by 11.06%, 6.38%, and 0.28%, respectively, while its kappa coefficient was comparable to that of XGBoost but 0.14 and 0.08 higher than SVM and DT, respectively. These results suggest that RF outperforms SVM, DT, and XGBoost in terms of classification performance in this experiment.

Table 7. Comparison of classification accuracy of different methods based on RFECV.

Classifier	SVM	DT	XGBoost	RF
OA (%)	84.26	88.94	95.04	95.32
Kappa	0.80	0.86	0.94	0.94

Using the optimal feature set, this study applied SVM, DT, XGBoost, and RF to classify and extract various land cover types in the study area. The results show that RF achieved the best classification results, accurately extracting land cover with clear edges, closely matching the actual situation. In contrast, the classification accuracy of SVM, DT, and XGBoost was slightly lower than that of RF, as shown in Figures 8 and 9. In Figure 8, the overall classification performance of RF and XGBoost was similar. However, DT misclassified some bare soil as *Kobresia pygmaea* in certain areas, while SVM exhibited the poorest performance, with large-scale misclassification in the upper and middle parts of the study area. Figure 9 further demonstrates that RF provided the best classification results. XGBoost misclassified a small amount of bare soil as roads in certain areas, while DT misclassified a large amount of bare soil as roads, resulting in unclear road boundaries and some misclassification of vegetation. SVM failed to distinguish between bare soil with darker colors and *Kobresia pygmaea*, resulting in extensive misclassification along the edges of the road. Overall, RF performed the best in this study, followed by XGBoost, with SVM having the worst performance.

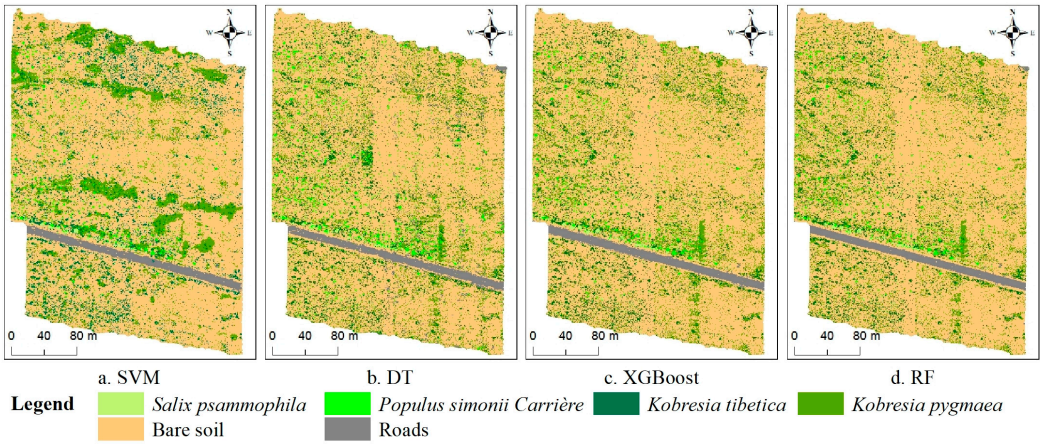


Figure 8. Classification results of different algorithms based on optimal feature set. (**a**) Support Vector Machine prediction result map in the study area, (**b**) Decision Tree prediction result map in the study area, (**c**) Extreme Gradient Boosting prediction result map in the study area, (**d**) Random Forest prediction result map in the study area.

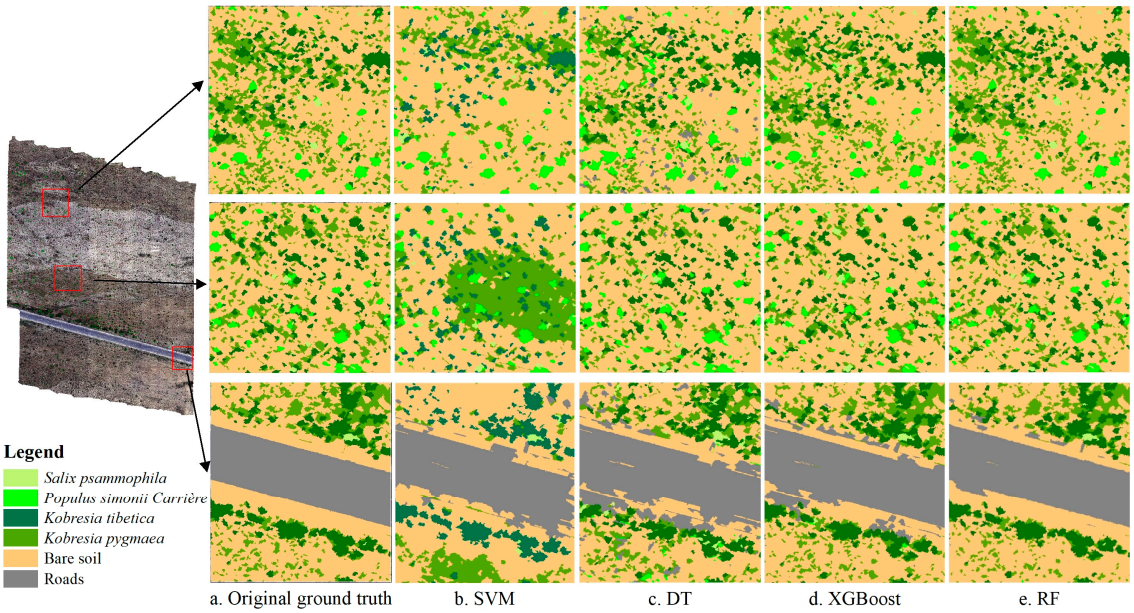


Figure 9. Detailed views of classification results from different algorithms based on optimal feature set. (**a**) Manual visual interpretation map, (**b**) Support Vector Machine prediction result map for part of the study area, (**c**) Decision Tree prediction result map for part of the study area, (**d**) Extreme Gradient Boosting prediction result map for part of the study area, (**e**) Random Forest prediction result map for part of the study area.

4. Discussion

This study used four machine-learning models to comprehensively investigate the impact of different spectral features and their combinations from visible and near-infrared bands on the classification accuracy of plateau vegetation. When only visible spectral features were used, *Salix psammophila* was often misclassified as *Populus simonii Carrière* and *Kobresia tibetica*. This misclassification is primarily due to the similarity in spectral characteristics among these three plants, related to the content of pigments such as carotenoids, chlorophyll, and xanthophylls in their cells. These pigments are crucial for photosynthesis, as they absorb sunlight and convert it into chemical energy. The concentration of these pigments directly affects the color and spectral characteristics of the plants [58]. Adding HEIG reduced the misclassification rate between *Populus simonii Carrière* and *Salix psammophila*. Although these two species are similar in height, they exhibit significant differences in their near-infrared spectra, as the near-infrared spectrum reflects changes in the internal structure of their leaves and is closely related to water content and tissue characteristics [59]. Therefore, even when there is similarity in the visible spectrum, the near-infrared spectrum can still provide effective information to distinguish different types of vegetation, thereby improving classification accuracy. To further improve classification accuracy, vegetation indices that are critical for vegetation classification were introduced [41]. The study found that *Kobresia tibetica* and *Kobresia pygmaea* showed significant differences in visible light indices, while *Populus simonii Carrière* and *Salix psammophila*, as well as *Kobresia tibetica* and *Kobresia pygmaea*, differed in near-infrared indices. Both types of index features contribute to overall classification accuracy, but the contribution of the near-infrared index is more significant. In addition, simultaneously introducing visible and near-infrared indices is more effective than using a single index; the combination of indices can capture richer information. This is because high-dimensional features can extract more information related to the physiological characteristics and environmental adaptability of vegetation, helping the model more accurately identify different vegetation types. Additionally, combining multiple indices can reduce the potential information redundancy of a single index, enhancing the model's stability and robustness. Therefore, texture features commonly used in object-oriented classification are also introduced [34]; however, their contribution to

classification accuracy was limited. As shown in Figure 6, the contribution rate of texture features is generally low, which may be due to the indistinct texture characteristics of the vegetation in the region. An excess of texture features can lead to data redundancy, consequently affecting model performance. Feature selection can effectively remove redundant features, reduce noise interference, and improve the classification performance of the model [60]. In this study, relevant features for highland vegetation classification were selected using feature selection methods from four feature sets: SPEC, INDE, HEIG, and GLCM. The experimental results show that feature selection enhanced the overall model performance, with all models achieving their best classification accuracy on the selected feature set, with RF showing the highest accuracy. This is because the optimized feature set not only reduces the computational complexity of the model but also significantly enhances its generalization ability, making it more robust in identifying different vegetation types. By selecting feature subsets that are highly relevant to highland vegetation characteristics, the model's ability to extract key information is improved, ensuring the accuracy and reliability of the classification results. Therefore, implementing effective feature selection strategies is a crucial aspect of the fine classification of highland vegetation.

In summary, this study explored the effects of different features and their combinations on plateau vegetation classification using multiple machine-learning models. The results indicate that the combination of the optimal feature set and the RF model can effectively identify plateau shrubs and grasses. However, there are still some limitations in this study. Although UAV remote sensing has advantages such as speed and efficiency, and performed well in this study, it also has limitations, such as poor UAV endurance and limited image coverage. Future research can combine UAV imagery with satellite images for plateau vegetation classification to obtain large-scale, high-precision plateau vegetation data. Additionally, although multispectral UAV imagery was used as the research object, the image information obtained is still limited. To further enrich the image data, future research could explore the integration of hyperspectral imagery and LiDAR (Light Detection and Ranging) data. This combination can provide more comprehensive spectral information and three-dimensional terrain features, thereby enhancing the richness and complexity of the imagery. This approach not only aids in improving classification accuracy but also allows for better detection of subtle changes in vegetation and ecological characteristics, providing more precise and comprehensive support for the monitoring and protection of highland ecosystems.

5. Conclusions

This study used multispectral UAV imagery combined with SVM, DT, XGBoost, and RF models to investigate the role of near-infrared spectra in the fine classification of plateau shrubs and grasses. The results show that near-infrared spectra and related indices are crucial for identifying plateau plant species and can significantly improve classification accuracy: PA increased by 3.32~7.96%, UA increased by 1.42~3.66%, and OA increased by 0.57~1.98%. Moreover, feature selection effectively reduced redundancy in the high-dimensional feature set, further improving classification accuracy. All models achieved their best performance on the optimal feature set; OA increased by 1.14~2.13% compared to the previous results. Finally, the RF model, combined with the optimal feature combination and object-oriented classification methods, enabled the fine classification of plateau vegetation. It achieved the highest overall accuracy among the four models, with an OA of 95.32% and a kappa coefficient of 0.94. This study provides a solid foundation for the identification of plateau plant species and offers important references for future monitoring of plateau vegetation growth and ecological restoration.

Author Contributions: Conceptualization, X.C., H.D., and H.Z.; methodology, X.C., H.D., and H.Z.; software, X.C. and W.Z.; validation, W.Z.; analysis, X.C. and H.D.; investigation, H.Z., X.C., and W.Z; resources, X.C.; data curation, X.C. and H.D.; writing—original draft preparation, X.C. and H.D.; writing—review and editing, X.C., H.Z., and H.D.; visualization, X.C. and H.D.; supervision, W.Z.

and H.D.; project administration, H.D.; funding acquisition, H.D. All authors have read and agreed to the published version of the manuscript.

Funding: This work was supported by the Science and Technology Department of Tibet Key Project (XZ202201ZY0003G) and the Sichuan Education Department Natural Science Key Project (18ZA0047).

Data Availability Statement: The data presented in this study are available upon request from the corresponding author due to restrictions, e.g., privacy or ethics.

Acknowledgments: The authors would like to thank scikit-learn for the original RFECV code.

Conflicts of Interest: The authors declare that the research was conducted in the absence of any commercial or financial relationships that could be construed as a potential conflict of interest.

References

1. Du, Z.; Cong, N. Responses of vegetation and soil characterisitics to degraded grassland under different degrees on the Qinghai-Tibet Plateau. *Acta Ecol. Sin.* **2024**, *44*, 2504–2516. [CrossRef]
2. Yang, X.; Wang, J.; Chen, B.; Pu, Q. Quantitative characteristics of timberline vegetation on Mt. Shergyla, Tibet. *J. Beijing For. Univ.* **2011**, *33*, 6. [CrossRef]
3. Trautmann, T.; Koirala, S.; Carvalhais, N.; Güntner, A.; Jung, M. The importance of vegetation in understanding terrestrial water storage variations. *Hydrol. Earth Syst. Sci.* **2022**, *26*, 1089–1109. [CrossRef]
4. Sang, J.; Song, C.; Jia, N.; Jia, Y.; Liu, C.; Qiao, X.; Zhang, L.; Yuan, W.; Wu, D.; Li, L.; et al. Vegetation survey and mapping on the Qinghai-Tibet Plateau. *Biodivers. Sci.* **2023**, *31*, 22430. [CrossRef]
5. Zhang, H.; Zhu, W.; Shi, P.; Zhao, C.; Liu, R.; Tang, H.; Wang, J.; He, B. The differences of vegetation characteristics and environmental conditions among main vegetation types on the Qinghai-Tibet Plateau. *Acta Ecol. Sin.* **2024**, *44*, 2955–2970. [CrossRef]
6. Jiang, C.; Zhang, H.; Wang, X.; Feng, Y.; Labzovskii, L. Challenging the land degradation in China's Loess Plateau: Benefits, limitations, sustainability, and adaptive strategies of soil and water conservation. *Ecol. Eng.* **2019**, *127*, 135–150. [CrossRef]
7. Lin, Y.; Zhang, W.; Yu, J.; Zhang, H. Fine classification of urban vegetation based on UAV images. *China Environ. Sci.* **2022**, *42*, 2852–2861. [CrossRef]
8. Liu, E.; Zhao, H.; Zhang, S.; He, J.; Xiao, X. Identification of plant species in an alpine steppe of Northern Tibet using close-range hyperspectral imagery. *Ecol. Inform.* **2021**, *61*, 101213. [CrossRef]
9. Morrison, L.W. Observer error in vegetation surveys: A review. *J. Plant Ecol.* **2016**, *9*, 367–379. [CrossRef]
10. Laba, Z.; Laba, C. The Vegetation Classification Research of North Tibetan Plateau Based on MODIS. *Plateau Mt. Meteorol. Res.* **2010**, *30*, 18–21. [CrossRef]
11. Zhang, H.; Zhao, C.; Zhu, W. A new vegetation map for Qinghai-Tibet Plateau by integrated classification from multi-source data products. *J. Beijing Norm. Univ.* **2021**, *57*, 816–824. [CrossRef]
12. Chen, X.; Sun, Y.; Guo, S.; Duan, Y.; Tang, A.; Ye, Z.; Zhang, H. Urban Tree Species Classification by UAV Visible Light Imagery and OBIA-RF Model. *J. Northeast. For. Univ.* **2024**, *52*, 48–59. [CrossRef]
13. Song, E.; Zhang, Y.; Shao, G.; Liu, J.; Wang, Y.; Zhu, X. Classification of geological features in agricultural parks based on multispectral remote sensing by unmanned aerial vehicle. *Jiangsu J. Agric. Sci.* **2023**, *39*, 1862–1871. [CrossRef]
14. He, R.; Zhao, Y.; Wu, X.; Zhenqi, H. A review of UAV monitoring in mining areas: Current status and future perspectives. *Int. J. Coal Sci. Technol.* **2019**, *6*, 320–333. [CrossRef]
15. Dash, J.P.; Watt, M.S.; Pearse, G.D.; Heaphy, M.; Dungey, H.S. Assessing very high resolution UAV imagery for monitoring forest health during a simulated disease outbreak. *ISPRS J. Photogramm. Remote Sens.* **2017**, *131*, 1–14. [CrossRef]
16. Zhai, H.; Tang, B.; Gu, B. Classification of Slope Plant Species Based on Image of UAV. *J. Northwest For. Univ.* **2020**, *35*, 185–190. [CrossRef]
17. Zhang, Z.; Zhu, L. A Review on Unmanned Aerial Vehicle Remote Sensing: Platforms, Sensors, Data Processing Methods, and Applications. *Drones* **2023**, *7*, 398. [CrossRef]
18. Ye, Z.; Guo, Q.; Zhang, J.; Zhang, H.; Deng, H. Extraction of urban impervious surface based on the visible images of UAV and OBIA-RF algorithm. *Trans. Chin. Soc. Agric. Eng.* **2022**, *38*, 225–234. [CrossRef]
19. Jin, M.; Xu, Q.; Guo, P.; Han, B.; Jin, J. Crop Classification Method from UAV Images based on Object-Oriented Multi-feature Learning. *Remote Sens. Technol. Appl.* **2023**, *38*, 588–598. [CrossRef]
20. Ye, Z.; Yang, K.; Lin, Y.; Guo, S.; Sun, Y.; Chen, X.; Lai, R.; Zhang, H. A comparison between Pixel-based deep learning and Object-based image analysis (OBIA) for individual detection of cabbage plants based on UAV Visible-light images. *Comput. Electron. Agric.* **2023**, *209*, 107822. [CrossRef]
21. Huang, Y.; Lu, C.; Jia, M.; Wang, Z.; Su, Y.; Su, Y. Plant species classification of coastal wetlands based on UAV images and object-oriented deep learning. *Biodivers. Sci.* **2023**, *31*, 22411. [CrossRef]
22. She, J.; Shen, A.; Shi, Y.; Zhao, N.; Zhang, F.; He, H.; Wu, T.; Li, H.; Ma, Y.; Zhu, X. Vegetation classification of UAV remote sensing images in desert steppe based on object-oriented technology. *Acta Prataculturae Sin.* **2024**, *33*, 1–14. [CrossRef]

23. Geng, R.; Fu, B.; Cai, J.; Chen, X.; Lan, F.; Yu, H.; Li, Q. Object-Based Karst Wetland Vegetation Classification Method Using Unmanned Aerial Vehicle images and Random ForestAlgorithm. *J. Geo-Inf. Sci.* **2019**, *21*, 1295–1306. [CrossRef]
24. Na, M.; Li, Y.; Wang, W.; Ha, S.; Li, F.; Ha, S. Identification of typical species in desert steppe based on unmannedaerialvehicle multispectral images. *China Agric. Inform.* **2022**, *34*, 37–48. [CrossRef]
25. Yang, L.; Chen, Y.; Yue, D.; Feng, Z. Information extraction of urban green space based on UAV remote sensing image. *Sci. Surv. Mapp.* **2017**, *42*, 6. [CrossRef]
26. Li, H.; HE, J.; Ni, Z.; Zhou, B.; Li, Q.; Shen, W. A Study on TWINSPAN Classification of Meadow Plants in Lazi County, Tibet. *Acta Agric. Univ. Jiangxiensis* **2004**, *26*, 6. [CrossRef]
27. Cervantes, J.; Garcia-Lamont, F.; Rodríguez-Mazahua, L.; Lopez, A. A comprehensive survey on support vector machine classification: Applications, challenges and trends. *Neurocomputing* **2020**, *408*, 189–215. [CrossRef]
28. Costa, V.G.; Pedreira, C.E. Recent advances in decision trees: An updated survey. *Artif. Intell. Rev.* **2023**, *56*, 4765–4800. [CrossRef]
29. Belgiu, M.; Drăguţ, L. Random forest in remote sensing: A review of applications and future directions. *ISPRS J. Photogramm. Remote Sens.* **2016**, *114*, 24–31. [CrossRef]
30. Chen, T.; Guestrin, C. XGBoost: A Scalable Tree Boosting System. In Proceedings of the 22nd ACM SIGKDD International Conference on Knowledge Discovery and Data Mining, San Francisco, CA, USA, 13–17 August 2016; pp. 785–794. [CrossRef]
31. Wen, Y.; Zhao, J.; Lan, Y.; Yang, D.; Pan, F.; Cao, D. Classifications of Tree Species Based on UAV's Visible Light Images and Object-Oriented Method. *J. Northwest For. Univ.* **2022**, *37*, 74–80. [CrossRef]
32. Zhang, N.; Zhang, K.; Li, Y.; Li, X.; Liu, T. Study on Machine Learning Methods for Vegetation Classification in Typical Humid Mountainous Areas of South China based on the UAV Multispectral Remote Sensing. *Remote Sens. Technol. Appl.* **2023**, *38*, 163–172. [CrossRef]
33. Gao, H.; He, L.; He, Z.; Bai, W. Early landslide mapping with slope units division and multi-scale objectbased image analysis—A case study in the Xiansh.ui River basin of Sichuan, China. *J. Mt. Sci.* **2022**, *19*, 1618–1632. [CrossRef]
34. Drăguţ, L.; Csillik, O.; Eisank, C.; Tiede, D. Automated parameterisation for multi-scale image segmentation on multiple layers. *ISPRS J. Photogramm. Remote Sens.* **2014**, *88*, 119–127. [CrossRef] [PubMed]
35. Li, R.; Ye, S.; Bai, Z.; Nedzved, A.; Tuzikov, A. Moderate Red-Edge vegetation index for High-Resolution multispectral remote sensing images in urban areas. *Ecol. Indic.* **2024**, *167*, 112645. [CrossRef]
36. Zhao, J.; Yang, H.; Lan, Y.; Lu, L.; Jia, P.; Li, Z. Extraction Method of Summer Corn Vegetation Coverage Based on Visible Light Image of Unmanned Aerial Vehicle. *Trans. Chin. Soc. Agric. Mach.* **2019**, *50*, 232–240. [CrossRef]
37. Wang, X.; Wang, M.; Wang, S.; Wu, Y. Extraction of vegetation information from visible unmanned aerial vehicle images. *Trans. Chin. Soc. Agric. Eng.* **2015**, *31*, 152–159. [CrossRef]
38. He, C.; She, D.; Zhang, X.; Yang, Z. Research on vegetation index of small watershed in the Loess Plateau based on visible light image analysis. *Res. Agric. Mod.* **2022**, *43*, 504–512. [CrossRef]
39. Feng, C.; Zhang, W.; Deng, H.; Dong, L.; Zhang, H.; Zhao, Z. A Combination of OBIA and Random Forest Based on Visible UAV Remote Sensing for Accurately Extracted Information about Weeds in Areas with Different Weed Densities in Farmland. *Remote Sens.* **2023**, *15*, 4696. [CrossRef]
40. Baret, F.; Guyot, G.; Major, D.J. TSAVI: A vegetation index which minimizes soil brightness effects on LAI and APAR estimation. In Proceedings of the 12th Canadian Symposium on Remote Sensing Geoscience and Remote Sensing Symposium, Vancouver, BC, Canada, 10–14 July 1989.
41. Ao, D.; Yang, J.; Ding, W.; An, S. Review of 54 Vegetation Indices. *J. Anhui Agric. Sci.* **2023**, *51*, 13–21. [CrossRef]
42. Miura, T.; Huete, A.R.; Yoshioka, H. Evaluation of sensor calibration uncertainties on vegetation indices for MODIS. *IEEE Trans. Geosci. Remote Sens.* **2000**, *38*, 1399–1409. [CrossRef]
43. Daughtry, C.S.T.; Gallo, K.P.; Goward, S.N.; Prince, S.D.; Kustas, W.P. Spectral estimates of absorbed radiation and phytomass production in corn and soybean canopies. *Remote Sens. Environ.* **1992**, *39*, 141–152. [CrossRef]
44. Xue, J.; Su, B. Significant Remote Sensing Vegetation Indices: A Review of Developments and Applications. *J. Sens.* **2017**, *2017*, 1353691. [CrossRef]
45. Manspeizer, N.; Karnieli, A. Disentangling disturbances with nested hierarchy classification of Mediterranean garrigue/maquis shrub community compositions through remote sensing and GIS. *Ecol. Inform.* **2024**, *82*, 102728. [CrossRef]
46. Li, J.; Wang, M.; Wang, Y.; Zhan, S.; Duan, P. Vegetation information classification method considering UAV image point cloud characteristics. *Ecol. Sci.* **2022**, *41*, 11–18. [CrossRef]
47. Batool, F.E.; Khan, M.A.; Sharif, M.; Javed, K.; Riaz, N. Offline Signature Verification System: A Novel Technique of Fusion of GLCM and Geometric Features using SVM. *Multimed. Tools Appl.* **2020**, *83*, 14959–14978. [CrossRef]
48. Humeau-Heurtier, A. Texture Feature Extraction Methods: A Survey. *IEEE Access* **2019**, *7*, 8975–9000. [CrossRef]
49. Qi, G.; Yu, Z.; Shan, Y.; Tian, Y. Identification of rodent hole patches in desert grasslands using UAV imagery and OBIA-CFS algorithms. *Pratacultural Sci.* **2024**, *41*, 1–9. [CrossRef]
50. Wang, Y.; Li, S.; Dong, C.; Yang, G. Remote sensing information extraction for mangrove forests based on multi-feature parameters: A case study of Guangdong Province. *Remote Sens. Nat. Resour.* **2024**, *36*, 95–102. [CrossRef]
51. Zhang, G.; Wang, X.; Xu, X.; Yan, L.; Chang, M.; Li, Y. Desert Vegetation Classification Based on Object-oriented UAV Remote Sensing Images. *J. Agric. Sci. Technol.* **2021**, *23*, 69–77. [CrossRef]

52. Chen, C.; Liang, J.; Yang, G.; Sun, W.; Gong, S.; Wang, J. Remote sensing parameters optimization for accurate land cover classification. *Acta Geod. Cartogr. Sin.* **2024**, *53*, 1401–1416. [CrossRef]
53. Zhou, T. Object-Oriented Land Cover Classification Using High Spatial Resolution Remote Sensing. *Geomat. Sci. Technol.* **2020**, *8*, 9–16. [CrossRef]
54. Zhong, Y.; Li, J.; Han, J.; Shao, W. Identification of rice in Shangxing Town, Liyang City based on Sentinel image and multi-feature optimization. *Jiangsu J. Agric. Sci.* **2023**, *39*, 1688–1697. [CrossRef]
55. Wei, Y.; Yang, T.; Zang, S.; He, L.; Duan, J.; Feng, W. Monitoring Wheat Lodging Based on UAV Multi-Spectral Image Feature Fusion. *Sci. Agric. Sin.* **2023**, *56*, 1670–1685. [CrossRef]
56. Theissler, A.; Thomas, M.; Burch, M.; Gerschner, F. ConfusionVis: Comparative evaluation and selection of multi-class classifiers based on confusion matrices. *Knowl.-Based Syst.* **2022**, *247*, 108651. [CrossRef]
57. Petti, D.; Li, C. Weakly-supervised learning to automatically count cotton flowers from aerial imagery. *Comput. Electron. Agric.* **2022**, *194*, 106734. [CrossRef]
58. Bai, J.; Niu, Z.; Bi, K.; Wang, J.; Huang, Y.; Sun, G. Bi-Directional Reflection Characteristic of Vegetation Leaf Measured by Hyperspectral LiDAR and Its Impact on Chlorophyll Content Estimation. *Spectrosc. Spectr. Anal.* **2023**, *43*, 1598–1605. [CrossRef]
59. Wu, G.; Lai, M.; Wang, Y.; Lian, H. Review on Application of Near Infrared Spectroscopy in Plant Leaves. *For. Environ. Sci.* **2020**, *36*, 118–127.
60. Cao, Y.; Dai, J.; Zhang, G.; Xia, M.; Zhao, Q.; Mu, Z.; Xu, M. Remote sensing monitoring of non-agriculturalization in typical areas of the Northern Xinjiang of China based on feature optimization. *Trans. Chin. Soc. Agric. Eng.* **2024**, *40*, 275–286. [CrossRef]

Disclaimer/Publisher's Note: The statements, opinions and data contained in all publications are solely those of the individual author(s) and contributor(s) and not of MDPI and/or the editor(s). MDPI and/or the editor(s) disclaim responsibility for any injury to people or property resulting from any ideas, methods, instructions or products referred to in the content.